remote sensing

MDPI

Article

Ash Decline Assessment in Emerald Ash Borer Infested Natural Forests Using High Spatial Resolution Images

Justin Murfitt [1,†], Yuhong He [1,*,†], Jian Yang [2,†], Amy Mui [1] and Kevin De Mille [3]

1 Department of Geography, University of Toronto Mississauga, 3359 Mississauga Rd, Mississauga, ON L5L 1C6, Canada; justin.murfitt@mail.utoronto.ca (J.M.); amy.mui@utoronto.ca (A.M.)
2 Department of Geography, University of Toronto, 100 St. George Street, Toronto, ON M5S 3G3, Canada; jiangeo.yang@mail.utoronto.ca
3 Credit Valley Conservation, Mississauga, ON L5N 6R4, Canada; KDemille@creditvalleyca.ca
* Correspondence: yuhong.he@utoronto.ca; Tel.: +1-905-569-4679
† These authors contributed equally to this work.

Academic Editors: Angela Lausch, Marco Heurich, Nicolas Baghdadi and Prasad Thenkabail
Received: 2 November 2015; Accepted: 11 March 2016; Published: 17 March 2016

Abstract: The invasive emerald ash borer (EAB, *Agrilus planipennis* Fairmaire) infects and eventually kills endemic ash trees and is currently spreading across the Great Lakes region of North America. The need for early detection of EAB infestation is critical to managing the spread of this pest. Using WorldView-2 (WV2) imagery, the goal of this study was to establish a remote sensing-based method for mapping ash trees undergoing various infestation stages. Based on field data collected in Southeastern Ontario, Canada, an ash health score with an interval scale ranging from 0 to 10 was established and further related to multiple spectral indices. The WV2 image was segmented using multi-band watershed and multiresolution algorithms to identify individual tree crowns, with watershed achieving higher segmentation accuracy. Ash trees were classified using the random forest classifier, resulting in a user's accuracy of 67.6% and a producer's accuracy of 71.4% when watershed segmentation was utilized. The best ash health score-spectral index model was then applied to the ash tree crowns to map the ash health for the entire area. The ash health prediction map, with an overall accuracy of 70%, suggests that remote sensing has potential to provide a semi-automated and large-scale monitoring of EAB infestation.

Keywords: emerald ash borer; random forest; forest health; segmentation

1. Introduction

The emerald ash borer (EAB) (*Agrilus planipennis* Fairmaire) is an invasive wood-boring beetle that originated from Eastern Asia [1]. The EAB attacks and kills all species of native ash trees (*Fraxinus* sp.), which are widely distributed across the Great Lakes region of North America. Once established, this pest can cause an estimated 99% mortality in ash stands annually by damaging the critical (phloem) tissue that carries nutrients from the roots to the canopy [2,3]. The pest was first detected in Windsor, Ontario, and Detroit, Michigan, in 2002 [1]. Although the spread of EAB is not fast, it is accelerated through human intervention by the transportation of ash wood products and firewood [1,2]. A recent survey conducted in Canada indicates that EAB has already spread to 27 counties within Ontario and to seven areas within Quebec in a span of about ten years [1]. Continued spread of this pest could result in large-scale ash mortality, leading to serious ecological, economic, and social consequences in this region [4,5].

EAB infestation can be detected by a variety of symptoms shown by ash trees, including exit bore holes, canopy thinning, twig dieback, larval bore tracts under the bark, and evidence of increased

woodpecker activity [5–7]. The EAB will eventually cause the death of an ash tree; however, this can be a delayed response, meaning it can take three or four years for a mature tree to die [8]. Several methods have been developed to attempt to control and manage the spread of EAB [5]. These methods include containment procedures and injection of insecticides into early-infested trees [9]. However, to successfully employ these methods, an effective method of detecting early EAB infestation is required.

One important step in the management of EAB infestations is the identification of ash trees, which occupy a large proportion of both natural and urban forests in the Great Lakes region of North America. Geographic object-based image analysis (GEOBIA), with the capability of delineating individual tree crowns, can aid in this process [10]. GEOBIA involves two image processing steps: segmentation and classification [11]. In recent years, several segmentation algorithms, including multiresolution segmentation and multi-band watershed transformation, have been applied to delineate individual tree crowns [12]. Multiresolution segmentation is a bottom-up region-merging technique that uses multiple spectral bands and creates a final image segment from a few smaller image objects through numerous iterative steps that attempt to minimize the internal weighted heterogeneity within the segment [13]. On the other hand, a recently-proposed multi-band watershed transformation algorithm incorporates multiple spectral bands for individual tree crown delineation, which has the potential to form a complete boundary around an individual tree crown without any refinement [12]. One of the critical parameters in these segmentation algorithms is the segmentation scale, which determines intra-segment homogeneity and inter-segment heterogeneity [11]. However, manual selection of the appropriate segmentation scale can be ineffective and subjective due to the influence of human bias [14,15]. The use of a segmentation evaluation index is thus recommended, in order to quantitatively evaluate the quality of the segments. The recently-proposed segmentation evaluation index (SEI) is an appropriate choice, as it effectively recognizes overlap between segments and reference polygons and thus allows the selection of the most appropriate segmentation threshold to assess tree crowns [16].

The image classification step, using image objects instead of pixels, has also proven to be beneficial for individual tree species classification [17]. Many classification algorithms, both parametric and non-parametric, have been used in land use/land cover classification, including the maximum likelihood classifier, decision tree classifier, neural network classifier, support vector machine classifier, and random forest classifier [18]. In recent years, the random forest classifier has attracted growing attention, especially in the forestry community [19]. The random forest classifier is an "ensemble learning" algorithm consisting of many decision trees and outputting the class that is the mode of the classes output by individual trees [20]. In contrast to more traditional classification methods (e.g., the maximum likelihood classifier), the random forest algorithm is a typical non-parametric classifier; thus its success is less dependent, or not dependent, upon the parameter settings [21].

Remote sensing data and techniques can not only aid in ash tree identification, but also have the potential to monitor ash tree health status. When vegetation is stressed, chlorophyll content declines, followed by an increase in the breakdown of chlorophyll molecules, which in turn affects pigments in the leaves of the plants [22–24]. Several vegetation indices that use red, red-edge, and near-infrared, such as the Normalized Difference Vegetation Index (NDVI) [23], are sensitive to changes in chlorophyll and, therefore, have the potential to detect EAB infestations. Previous studies have also demonstrated the potential of remote sensing for monitoring ash health. For example, Pontius *et al.* identified ash health in EAB-infested natural forests in Michigan and Ohio using hyperspectral imagery and ground observations [25]. Zhang *et al.* identified EAB-infested ash trees in an urban area in Canada through texture information and vegetation indices derived from hyperspectral data [26]. More recently, multispectral data obtained from the WorldView-2 sensor were used to classify ash mortality as a result of a fungal pathogen in Europe [27].

Building on existing work, this paper examines the utility of a field- and remote sensing-based approach to detect EAB-infested ash trees in a natural mixed hardwood forest in Ontario, Canada. The three objectives of this work are to: (1) map ash tree crowns using multi-band watershed transformation and multiresolution segmentation, as well as random forest classification; (2) establish

an ash health score using field-observed EAB health symptoms and investigate its relation to remote sensing spectral indices; and (3) map the EAB infestation stages to identify areas of concern. Different from previous work, we test the effectiveness of two popular segmentation algorithms and classify ash trees in a hardwood forest using only 4-band multispectral images that could be accessed and analyzed by conservation authorities.

2. Data and Methods

2.1. Study Area and Study Sites

The study area (43.81°N, 79.93°W) is located in the Credit River watershed, in Southeastern Ontario, Canada. The watershed covers approximately 1000 square kilometers of land, contains a mix of both urban and natural areas, and includes several conservation areas and municipalities such as Mississauga, Orangeville, and Caledon. The Ken Whillans Resource Management Area within the watershed was selected for this work because it is a natural forested area experiencing early EAB infestation according to the Credit Valley Conservation group (Figure 1). The Ken Whillans Resource Management Area covers 1.08 km^2 and contains a mix of deciduous (*Populus* sp., *Acer* sp., and *Fraxinus* sp.) and coniferous trees (*Pinus* sp. and *Abies* sp.). Ash trees cover approximately 38% of the forested area at Ken Whillans.

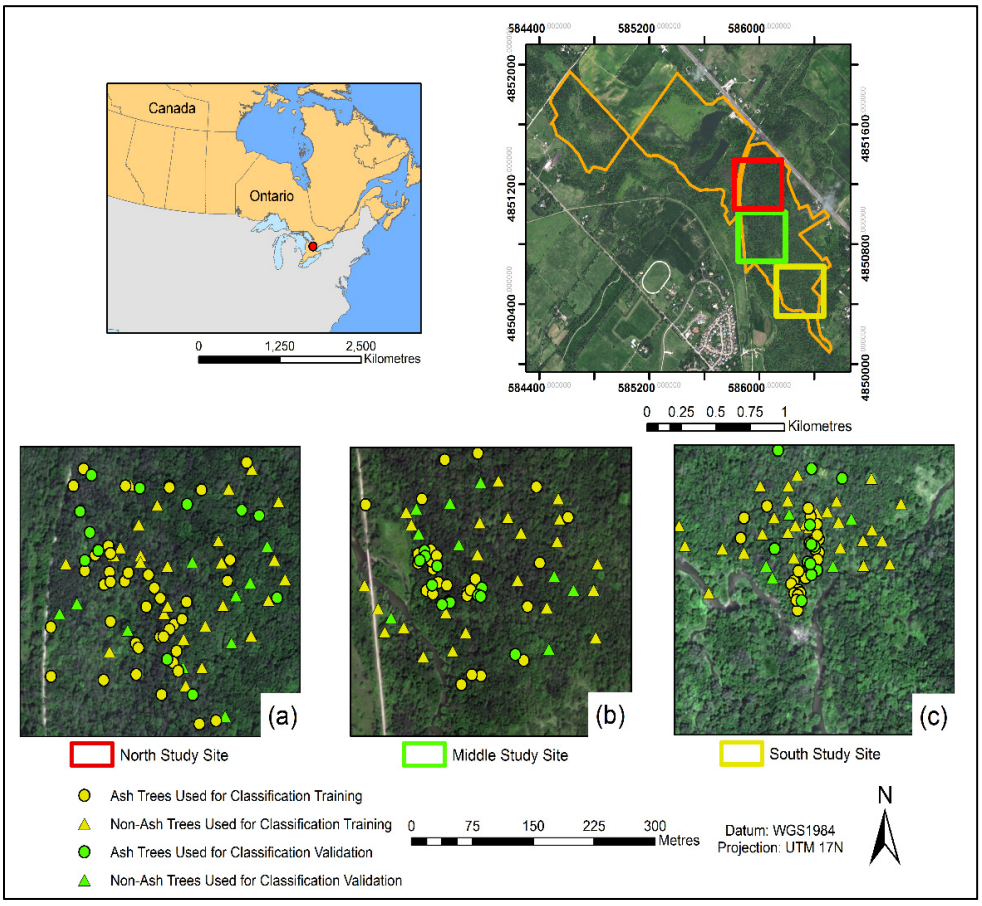

Figure 1. The three study sites within the Credit River Watershed ((**a**) is the north site; (**b**) is the middle site and (**c**) is the south site). The WorldView 2 image for the study area was displayed in true color composite (RGB: 321).

Three study sites—north, middle, and south sites—were selected to collect field data for this work (Figure 1). The north site is characterized by a large swamp area on the west side of the site, and comprised of many tall deciduous trees. The middle site has a large open field to the south

and a greater number of coniferous trees. The south site contains a larger number of shrubs and is more heterogeneous in terms of the tree species and canopy height. We did not select a site in the northwestern portion of the conservation area because this was not an area of concern according to Credit Valley Conservation. We split sites for data collection to allow for a comparison of segmentation methods over sites with different tree sizes and composition.

2.2. Study Data

2.2.1. Field Data

In 2014, a total of 53, 41, and 37 ash trees were identified in the north, middle, and south sites, respectively, based on morphometric characteristics (Figures 1 and 2). The tree locations were marked in the field using a Trimble GPS unit (Trimble Navigation Limited, Sunnyvale, CA, USA) with decimeter accuracy (Figure 1). In addition to the ash trees, a total of 32, 36, and 34 other dominant trees were recorded in the north, middle, and south sites, respectively, for classification purposes (Figure 1).

Figure 2. A collection of field pictures: (**a**) is ash tree bark as identified by the diamond-shaped pattern; (**b**) is an ash tree leaf as denoted by the tear drop shape and thin point; and (**c**) is a general photo of the mixed canopy.

Among the recorded ash trees, a total of 86 trees in the north and middle sites were randomly selected in 2015 to collect ash tree health status in relation to EAB symptoms when trees were in full canopy, between July and August (Figure 3). We could not collect tree health status data for the south site due to its temporal inaccessibility.

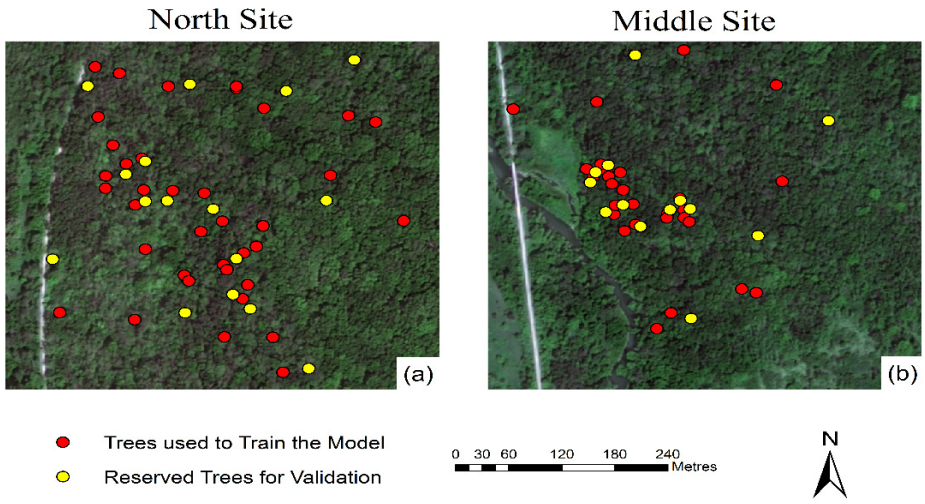

Figure 3. Out of the observed 86 ash trees, 57 trees (red dots) were used for establishing the tree health prediction model and 29 trees (yellow dots) were used for model validation. Only the north site (**a**) and middle site (**b**) were visited for tree health data, and no data were collected for the south site because of its inaccessibility.

The specific ash tree health variables we surveyed included twig dieback, crown condition/thinning, general tree health (a measure that considers bore holes, evidence of woodpecker activity, and epicormic branching), and crown transparency. All qualitative variables were collected on a scale from 1 to 10, with 10 indicating little decline in ash health, and 1 indicating severe decline in ash health. Values of 0 were all given to those trees that were completely dead. All data were collected by the same field team and cross-validated within the team members in order to limit user bias on the rating scale. The procedures to obtain these data were based on techniques employed by the United States Department of Agriculture [28], and are briefly described below.

Twig dieback measurement was obtained by visually inspecting the branches within the canopy of the ash tree. All visible branches were included in the determination of this measure, and it included both fine twig and branch mortality. Branches that were missing leaves were identified, and, depending on the percentage of dieback within the canopy, the tree was assigned to one of ten classes [28]. Each class represented a distinct 10% threshold between 0% and 100%. Crown thinning was evaluated by inspecting the various gaps in the crown [28]. This provided insight into how many and how large gaps were in the crown structure. The gaps were defined as holes and open space within the tree crown. These gaps were differentiated from natural gaps by looking at the location of gaps in relation to dead branches and twigs. The tree crown gaps that were related to twig dieback were determined to be the result of infestation. Gaps are present in most tree crowns; however, by looking at the relationship to dead branches, we can determine if they are indeed the result of infestation. The tree was then assigned into one of ten categories established for this symptom (Table 1).

Table 1. Ash tree classes based on crown gaps.

Crown Condition Classes	Parameters for Crown Gap Assignment
10	Little to no gaps in the crown
9	Small gaps in isolated sections of the crown
8	Small gaps throughout the crown
7	Larger gaps in isolated sections of the crown
6	Larger gaps throughout the entire crown
5	Large gaps in the crown
4	Large gaps cover more of the crown than leaves
3	Little evidence of a crown (some leaves)
2	Very few leaves, dispersed throughout the crown
1	Almost no leaves, little evidence of growth
0	Tree is dead

General tree health was evaluated through an investigation into the various EAB-specific symptoms displayed by the tree. This measure took into account twig dieback and crown thinning to a certain degree, but focused more on the observation of EAB bore holes, woodpecker activity, and epicormic branching, all of which are indicators of EAB infestation used in previous studies [6,7,29]. Trees were assigned to one of ten categories established for this measure of tree health, as indicated in Table 2.

Canopy transparency was measured using hemispherical photography. Different from traditional photos, which are commonly used for determining species composition and canopy cover, hemispherical photographs provide information on the light regime of the forest, which can be used to draw conclusions about the overall health of the canopy area [30]. A Canon Coolpix camera and stabilizing fisheye lens, mounted on a tripod, were used to take a minimum of eight photographs of the canopy around each tree. These images were processed using CAN_EYE software, version 6.3.1.2 (IRNA, Avignon, France), to produce a gap fraction and leaf area index, which has been demonstrated to be effective in previous studies on agricultural crops and oak tree health [31,32]. The software required a minimum input of eight images to perform a supervised classification and subsequent analysis of percent sky and vegetation for each tree (Figure 4. The classification results of this process were scaled from 0 to 10 by normalizing the data (Equation (1)).

$$Transparency\ Score = \frac{x_i - \min(x)}{\max(x) - \min(x)} \quad (1)$$

where xi is the classification percent produced by CAN_EYE, min(x) is the minimum score, and max(x) is the maximum classification data. This was used to quantify the amount of canopy dieback and overall canopy thinness, a symptom of Emerald Ash Borer infestation.

Table 2. Ash tree classes for general tree health.

Health Classes	Parameters for General Health Assignment
9 or 10	Crown is in good health, no evidence of twig dieback or slight, bark is healthy, no evidence of obvious EAB infection.
7 or 8	Crown is slightly different from a tree that received a 9 or 10. There may be small gaps in the crown (larger gaps for a 7). Bark may be peeling lightly and there may be trace amounts of evidence of EAB infection.
5 or 6	Crown is less full. There are medium-sized gaps in the crown and significant twig dieback. There is evidence of epicormic branching on the lower truck of the tree, and moderate evidence of EAB infection.
3 or 4	There is significant crown thinning and twig dieback. There is obvious evidence of EAB.
1 or 2	There is significant crown thinning and twig dieback. There is significant evidence of EAB.
0	0 is only given if the tree is dead.

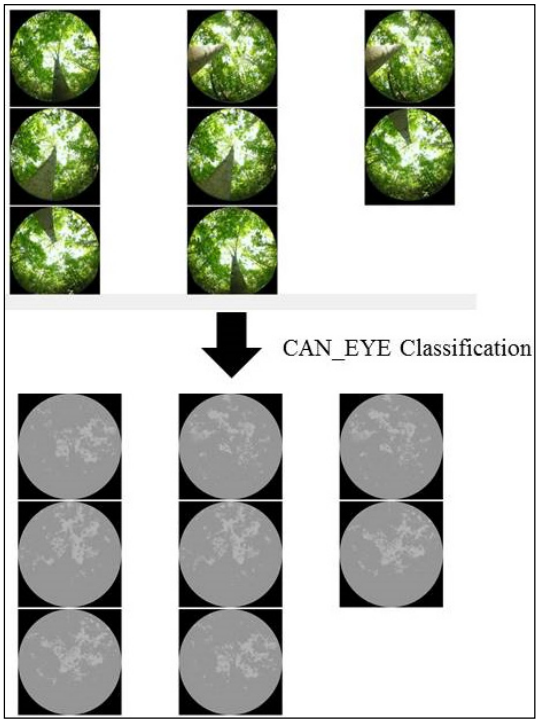

Figure 4. The process for hemispherical photography classification using CAN_EYE software. Eight images were imported into the software and the outer edges of the images were masked out. From this, the images were classified into percent vegetation and percent sky (gaps). The tree used in this figure has 87.3% vegetation cover and 12.7% open canopy.

2.2.2. Development of an Ash Health Score Based on Field Observations

The final ash health score was calculated by averaging the score from each of the collected ash health parameters, which were ranked from 0 to 10. This provided an overall ash health score for each tree that was studied within the different sites. Similar methods were used by Pontius *et al.* when predicting ash decline due to the emerald ash borer in Michigan [25].

2.2.3. Image Data

The WorldView-2 (WV2) image for the study sites was acquired on 13 September 2013. The image contained four multispectral bands (blue, 450–510 nm; green, 510–580 nm; red, 630–690 nm; and near infrared, 770–895 nm) with a spatial resolution of 2 meters, and a panchromatic band (450–800 nm) with a spatial resolution of 0.5 meters. The image was georeferenced using ground control points (RMSE = 0.44) and atmospherically corrected using the ATCOR surface reflectance module in Geomatica software (PCI GEOMATICS, Markham, ON, Canada). Image pan-sharpening was then implemented using the Graham-Schmidt method [33] to increase the spatial resolution and enable a more accurate identification of individual trees in the process of image segmentation. The Graham-Schmidt image pan-sharpening method was selected because it has been demonstrated to be effective at maintaining spectral information in comparison with other techniques, such as the IHS (intensity, hue, saturation) and SFIM (smoothing filter-based intensity modulation) techniques [34]. The pan-sharpened image was further clipped into three study sites for further analysis (Figure 1).

2.3. Methods

An overview of the workflow process used in this study is shown in Figure 5. To map ash tree health status, we first identified and delineated the ash trees from the remote sensing image; this was accomplished through segmentation and subsequent supervised classification. Next, we created an ash health index using field-observed ash tree data, and established an ash index-remote sensing spectral index regression model for the prediction of ash health. Finally, the ash health model was applied to the remote sensing image within the ash masks (classified ash trees) created in the first step to predict ash health.

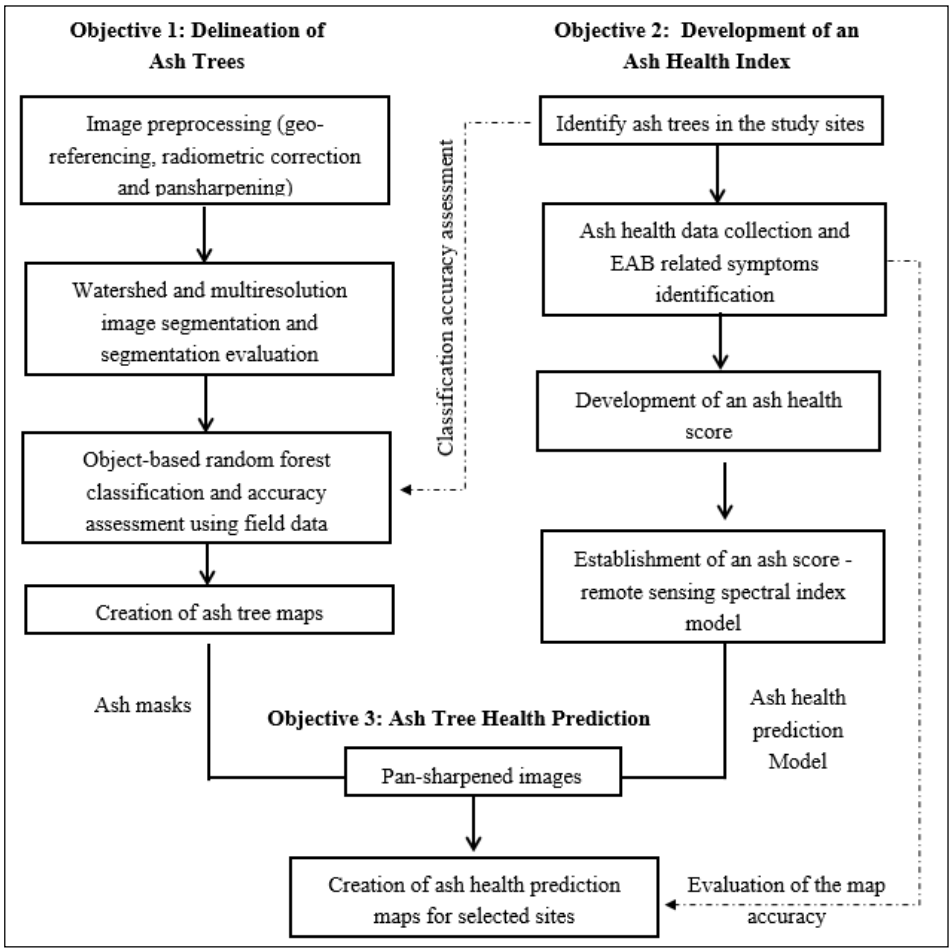

Figure 5. A complete workflow for mapping ash trees and predicting EAB infestation stages.

2.3.1. Image Segmentation and Classification

We employed the multi-band watershed segmentation [12] and multiresolution segmentation [35] algorithms to delineate tree crowns. The multi-band watershed segmentation algorithm uses a spectral angle metric to produce the gradient image and then segments the gradient image to match the boundary of the real world object. The equation for calculating the spectral angle is provided below:

$$\theta_{ab} = cos^{-1} \frac{\sum_{i=l}^{n} a_i b_i}{\sqrt{\sum_{i=l}^{n} a_i \sum_{i=l}^{n} b_i}} \quad (2)$$

where n is the number of spectral bands, and a_i and b_i are the reflectance components of two different pixels [12]. The watershed method produces a high degree of over-segmentation during the initial segmentation [12]. A seed-to-saddle difference threshold was then used to merge the over-segments in the SAGA (System for Automated Geoscientific Analyses) [36]. In this study, the values of the seed-to-saddle difference threshold between 0.05 and 0.5 were selected at a 0.05 interval.

The multiresolution algorithm implemented in eCognition Developer (Trimble Munich, Munich, Germany) was mainly controlled by several user-defined parameters, namely scale, shape, compactness, and layer weight [13]. The scale parameter, as the most important parameter, determines when to stop the merging process based on the heterogeneity threshold, which also takes into account the shape and compactness parameters [13]. The multiresolution method archives the segmentation process through local-oriented region merging, where the iteration process does not cease until the heterogeneity threshold exceeds the scale parameter. After careful trial-and-error attempts, we constrained the scale parameter between 3 and 12 by an interval of 1 for this application. Both the shape and compactness parameters were fixed at the values of 0.9 in order to produce the most optimal crown shapes [37]. Moreover, all the spectral bands were weighted equally for the segmentation.

The segmentation results derived from the two aforementioned algorithms were evaluated by the SEI method [16]. A lower value of SEI indicates a higher quality of image segmentation, and vice versa [11]. A total of 150 reference tree crowns (50 for each site) were manually delineated using the panchromatic image for segmentation assessment, and the scale parameter of the best segmentation was optimized by the lowest value of SEI.

The random forest classifier was then applied to classify the ash trees using the best segmentation product from each segmentation algorithm. The mean values of each spectral band were calculated as the representative features of each segment for classification. We implemented random forest classification (*i.e.*, random trees) in eCognition Developer. We conducted the classification in a hierarchical manner. The entire imagery was first classified into forest and non-forest areas (e.g., water, grass, bare land). The forest areas were then further classified into ash and non-ash trees. We selected 96 ash (out of 131) and 77 non-ash (out of 102) trees as the training samples to differentiate the ash and non-ash trees for the entire study area, and used the remaining samples to assess classification accuracy. The user's accuracy (UA), producer's accuracy (PA), and overall accuracy were derived from the confusion matrix to quantitatively evaluate the classification accuracy. PA indicates the accuracy of the classification in relation to the number of trees correctly classified over the ground truth points. UA denotes the number of correctly classified trees over the number of total points that were classified.

2.3.2. Establishing the Ash Health Prediction Model and Mapping the EAB Infestation

Seven remote sensing spectral indices, including the normalized difference vegetation index (NDVI), green normalized difference vegetation index (GNDVI), enhanced vegetation index (EVI), infrared percentage vegetation index (IPVI), difference vegetation index (DVI), ratio vegetation index (RVI), and renormalized difference vegetation index (RDVI), were calculated using spectral information extracted from the multispectral image (Table 3 [38–44]). These indices were selected because they have been used to evaluate vegetation health in previous studies [27,45].

The field-observed tree health data were split into two sets, 66 percent (57 ash trees) being used to create the model and 34 percent (29 ash trees) reserved for validation purposes (Figure 3). Linear regressions were calculated using the model fitting function in R software package (version 3.0.2) [46]. The spectral index with the lowest root means square error (RMSE, Equation (3)) for the validation data was selected as the final model for ash tree health prediction. The final model was then applied to the areas classified as ash within the different sites on a pixel-by-pixel basis to predict ash health within the conservation area. The overall accuracy of the ash health model was determined by the measure of map accuracy (MA, Equation (4)) [47]:

$$RMSE = \sqrt{\frac{1}{n}\sum_{i=1}^{n}(x_i - \hat{x}_i)^2} \quad (3)$$

$$MA = \left(1 - \frac{RMSE}{mean}\right) x\ 100 \quad (4)$$

where x is the observed ash health score, $\hat{x}$ is the predicted ash health score, n is the number of observations, and mean is the average of predicted ash health score.

Table 3. All remote sensing vegetation health indices used as initial independent variables to the regression model. B = Blue, G = Green, R = Red, and NIR = Near Infrared.

Remote Sensing Index	Index Formula	Reference
NDVI	(NIR − R)/(NIR + R)	[38]
GNDVI	(NIR − G)/(NIR + G)	[39]
EVI	2.5 × ((NIR − R)/(NIR + R × 6.0 − 7.5 × B + 1)	[40]
IPVI	(NIR)/(NIR + R)	[41]
DVI	(NIR − R)	[42]
RVI	(NIR/R)	[43]
RDVI	$\sqrt{}$(NDVI × RVI)	[44]

3. Results and Discussion

3.1. Segmentation Results

The lowest SEI occurred at the threshold of 0.25 (SEI = 0.45) for the watershed segmentation and at the scale of 7 (SEI = 0.58) for the multiresolution segmentation in the north site, 0.15 (SEI = 0.41) for watershed and 8 (SEI = 0.61) for multiresolution in the middle site, and 0.15 (SEI = 0.43) for watershed and 5 (SEI = 0.58) for multiresolution in the south site (Figure 6). The substantially lower SEI and closely-approximated tree crown segments (Figure 7) created by the watershed segmentation algorithm suggest that the watershed algorithm is more effective at segmenting the mixed hardwood forest imagery.

The optimal segmentation thresholds/scales differ slightly between sites, likely due to the difference in species composition and tree crown size between sites. The optimum watershed segmentation threshold of 0.25 in the north site is slightly higher than the optimal threshold of 0.15 in the middle and south sites. This result is consistent with field observations that the north site is dominated by deciduous trees with a larger mean crown size and, as a result, a higher segmentation threshold. When the image was segmented for the entire area, the watershed threshold of 0.25 created the best segmentation map with the lowest SEI of 0.45, while the multiresolution scale of 8 produced the lowest SEI of 0.56. These results indicate that using a fixed, global scale parameter to control the process of the entire image segmentation can capture the full range of variation in the size of geo-objects. As a result, we chose the entire area segmentation product from each method for the subsequent classification practice.

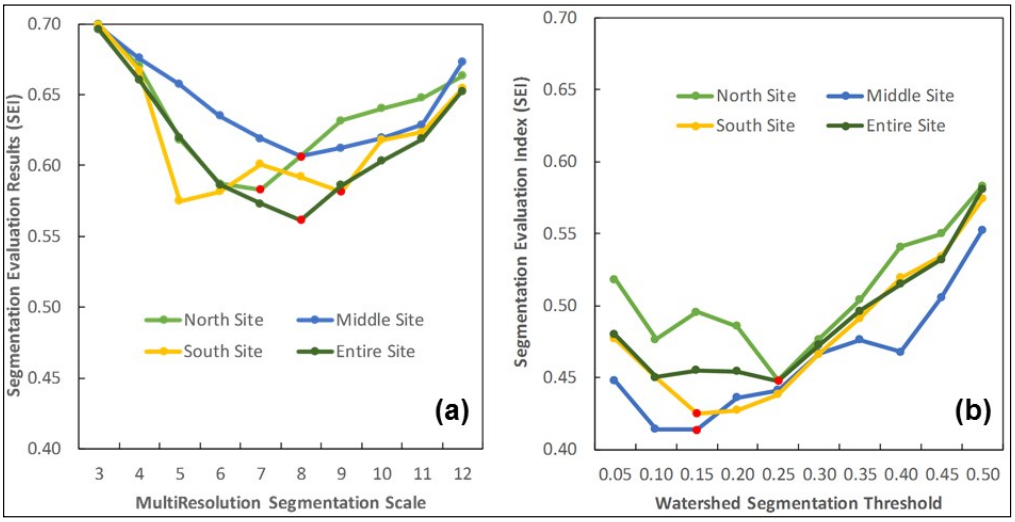

Figure 6. The segmentation accuracy as a function of the segmentation threshold or scale. The lower the segmentation evaluation index, the better the particular scale or threshold value is at segmenting the image. (**a**) shows the results of the multiresolution segmentation and (**b**) shows the results of the watershed segmentation. The red dots in the lines indicate the optimal scales/threshold with the lowest SEI for that image.

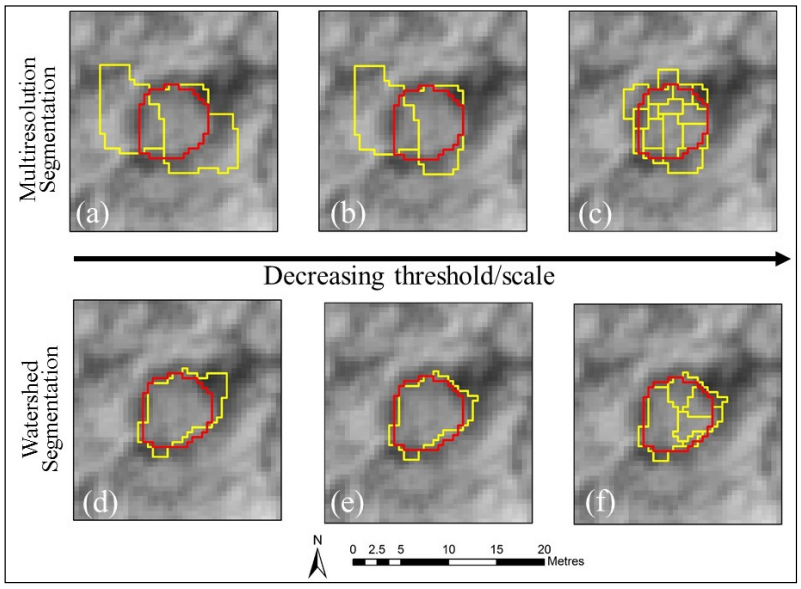

Figure 7. (**a**–**f**) The size of segments created by watershed and multiresolution algorithms change as a function of the scale/threshold. Reference polygons are in red and segments are in yellow. (**a**) and (**d**) are segments created by a larger threshold/scale value (0.5 for watershed and 12 for multiresolution); (**b**) and (**e**) are the best segment threshold/scale values (0.25 for watershed and 8 for multiresolution); (**c**) and (**f**) are the smallest segments created by the two methods (0.1 for watershed and 4 for multiresolution).

The effect of increasing or decreasing scale or threshold on the resulting segment is demonstrated in Figure 7. When the threshold is too large, the generated segments are greater than the reference polygon, and when the threshold is too small, over-segmentation occurs, whereby the resulting image segment is smaller than the reference polygon. A threshold value of 0.25 most closely matches the reference tree crown polygon when using the watershed segmentation approach (Figure 7a–c). Similar patterns to those observed with multiresolution segmentation for under- and over-segmentation are

also observed in the multiresolution segmentation images (Figure 7d–f). Overall, the watershed method provides a better shape of the object.

3.2. Classification Results

Classification was conducted on the best watershed segmentation created by the threshold of 0.25 and the best multiresolution segmentation produced by the scale parameter of 8. Visual interpretation of classification maps (Figure 8) indicates that the ash trees spread out in small clusters in all sites, which is very similar to what was observed in the field, as there were small groves of ash trees surrounded by larger clusters of other coniferous and deciduous trees. The watershed segmentation-based classification produced an overall accuracy of 63.3%, slightly higher than the 60.0% overall accuracy of multiresolution segmentation-based classification (Table 4). When focusing on the ash tree class, the watershed segments-based classification resulted in a user's accuracy of 67.6% and a producer's accuracy of 71.4% for ash trees. In comparison, the classification based on multiresolution segmentation produced a similar user's accuracy (67.7%), but much lower producer's accuracy (60.0%). The results suggest that better segmentation could lead to higher classification accuracy in this application.

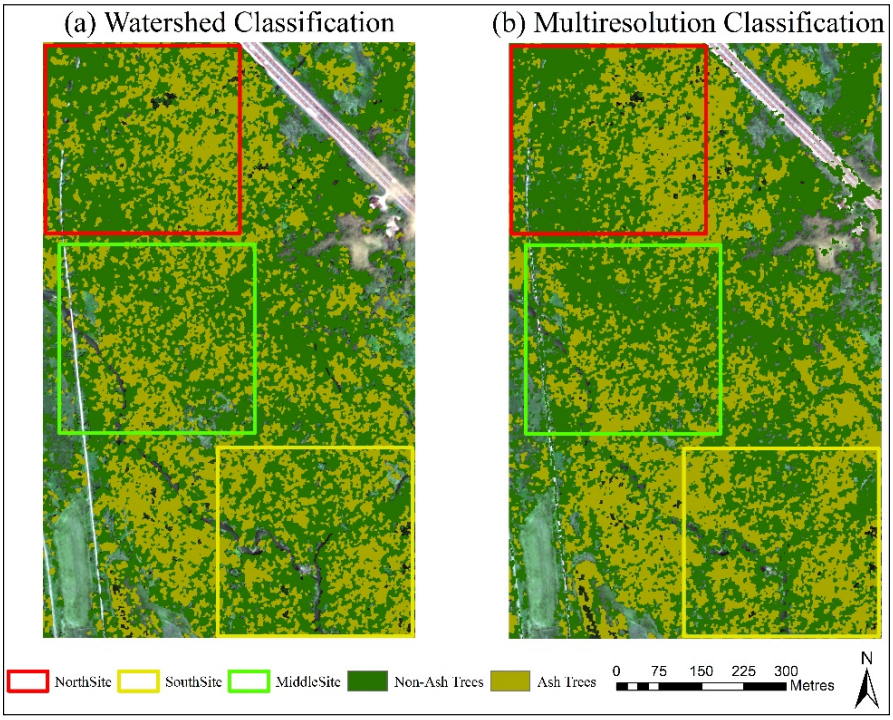

Figure 8. Classification maps from the watershed (**a**) and multiresolution (**b**) segmentations.

Table 4. Classification accuracy matrices for the ash and non-ash trees.

	Watershed-Based Classification				**Multiresolution-Based Classification**			
	Ash	**Non-Ash**	**Total**	**UA**	**Ash**	**Non-Ash**	**Total**	**UA**
Ash	25	12	37	67.6%	21	10	31	67.7%
Non-Ash	10	13	23	56.5%	14	15	29	51.7%
Total	35	25	60		35	25	60	
PA	71.4%	52.0%			60.0%	60.0%		
	Overall accuracy		63.3%		Overall accuracy		60.0%	

For the watershed segmentation-based classification, the user's accuracy is lower than the producer's accuracy for ash class, indicating there is a higher error of commission (1-user's accuracy)

than error of omission (1-producer's accuracy) when classifying ash trees. This is to be expected because the forest is comprised of several species of broadleaf trees that can be confused with ash trees. Two examples of these trees are the *Acer negundo* (Manitoba Maple) and *Ulmus* sp. (Elm tree). The clustering of trees in natural forests would also make it more difficult to differentiate between species. A study conducted using WV2 products to classify tree species in Kuala Lumpur experienced similar issues [48]. Fortunately, the users, in this case the conservation agencies, are less concerned with commissions but more concerned with omissions, because omission means that the ash trees are excluded from the species inventory and would prevent the conservation agencies from saving those omitted ash trees under early infestation

Our results show an improvement over a similar work that classified Asian ash (*Fraxinus mandschurica*) trees with an accuracy of 42% using IKONOS images in a mixed northern forest [49]. However, if comparison is made in terms of image wavelength used, the usefulness of an 8-band WV2 image is clear. The ash classification accuracy of 63.3% in this study is lower when compared with another work that produced an 82% ash identification accuracy using 8-band WV2 multispectral data [27]. A few more examples also demonstrate the usefulness of 8-band WV imagery. A classification work using WV imagery resulted in overall accuracies as high as 96% when classifying four tree species and 82% when classifying 10 species [50]. A study evaluating riparian vegetation using six bands of the WV2 achieved high overall accuracies of 93% [51]. Research mapping endangered tree species using WV imagery resulted in an accuracy of 77% [52]. In addition, hyperspectral imagery coupled with SVM showed high overall accuracies of 90% for delineating boreal forest areas that contain similar tree species to forests in our research [53]. Future work using higher spectral resolution imagery could expand on our current research to produce better species-level classification and thus provide a better understanding of the composition of the forest. This is supported by work done in urban areas that shows the direct benefits of using the 8-band WV2 products over both 4-band WV2 products and other high resolution products, such as IKONOS images [54].

3.3. Ash Health Prediction

Ash health prediction models were established using the selected indices. Model evaluation for all tested indices (Table 5) indicate that NDVI best predicted ash health over the study sites (root mean square of 2.01, $p < 0.01$, R^2 of 0.38) (Figure 9). DVI had a lower RMSE; however, it had a much lower R^2 value and a higher p value. Using the RMSE calculated from the reserved field data, the ash health map achieved an overall accuracy of 70% (Table 6). A breakdown of prediction accuracy by tree health class indicates the prediction algorithm becomes less accurate when ash becomes more severely infested (Table 6). This is expected, as the study area was experiencing early to moderate infestation and we have had limited training and validation data for severely infected trees. As shown in Table 6, only 5 out of 29 reference ash trees were recorded under a health score of 4.5. This result suggests that our approach would work well for detecting/predicting early EAB infestation, which is critically important for employing pest management methods effectively. However, more field data need to be collected in regions of more severe/long term EAB infestation to improve the model accuracy.

Table 5. Model evaluation parameters (R^2, significance value, and RMSE = root mean square error) for all indices tested. The results show that NDVI was the best model.

Index	R^2 Value	Significance Value	Validation RMSE
NDVI	0.38	<0.01	2.01
GNDVI	0.33	<0.01	2.19
EVI	0.28	<0.01	2.01
IPVI	0.38	<0.01	2.01
DVI	0.23	<0.01	1.97
RVI	0.34	<0.01	2.07
RDVI	0.36	<0.01	2.05

Table 6. A breakdown of ash classification accuracy by tree health class.

Health Score Class	Observed Health Score	Predicted Health Score	Reference Points	RMSE Per Class	Map Accuracy Per Class
2.5–3.5	3.09	5.92	2	2.86	51.6%
3.5–4.5	3.93	7.09	3	3.75	47.2%
4.5–5.5	4.99	6.48	8	4.03	37.8%
5.5–6.5	5.79	6.45	3	2.51	61.0%
6.5–7.5	7.28	6.77	1	1.61	76.3%
7.5–8.5	7.93	6.73	9	1.19	82.3%
8.5–9.5	8.94	7.20	3	1.18	83.7%
Overall RMSE		2.01	Overall Map Accuracy		70.0%

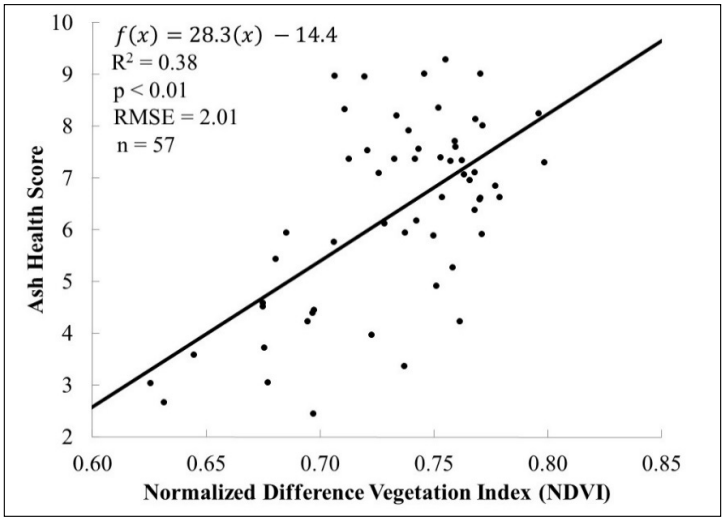

Figure 9. The relationship between the vegetation index NDVI and the ash health score.

Our overall accuracy is acceptable, but lower than that of a similar study which reported an accuracy of 97% when predicting ash health using hyperspectral data [25]. In terms of multispectral data, many studies used the 8-band WV2 imagery to predict health decline due to invasive species and found it achieved better prediction power. For example, a study on the bronze bug in South Africa produced a R^2 of 0.71 through the use of the red-edge and near-infrared bands in 8-band WV imagery [55]. Work done in Europe on the classification of health decline due to a fungus produced an overall accuracy of 77% [27]. A similar accuracy of 76% was obtained when investigating the early detection of bark beetle in Norway spruce [56]. Work conducted in Northern Chile also highlighted the success of using the red-edge band in combination with the near-infrared band [57]. These studies show the importance of the red-edge band when monitoring the health of vegetation species [58]. However, due to constraints in budgets for most conservation authorities, it is more practical to use the 4-band product, which our results show is an acceptable alternative.

In the predicted ash health map, areas with very low health scores cover small portions of the total study area for all three sites (Figure 10). The majority of ash trees are experiencing a moderate level of health to very slight levels of health decline. Within sites, ash health condition varies spatially. For the north site, a heavier infestation is taking place on the west side of the site, while the ash trees on the east side remain fairly healthy. The middle site shows a slight consistent decline throughout the area, with some lower amounts of decline identified on the west site of the site along the river. The south site shows evidence of some heavy decline, especially in the northern part, while the rest of the ash trees appear relatively healthy. These results are consistent with field observations, and with the assessment from the Credit Valley Conservation group (personal communication) that the entire area is undergoing the early stages of infestation.

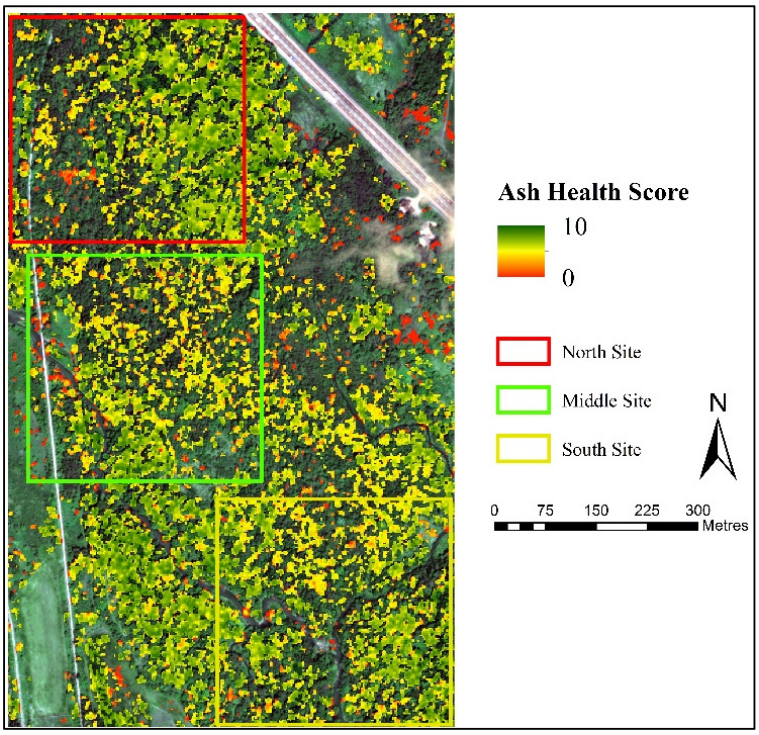

Figure 10. The ash health prediction map for the entire area.

The final ash health prediction products should be used with caution, due to the health decline map being produced based on the classification maps, which had about 33% errors of omission (meaning that some ash trees were confused with other trees, and not included in the prediction of ash health). We would also like to point out that, although the goal of this map was to identify EAB infestations, other disturbances such as an ice storm may have contributed to ash decline [22,59,60]. However, the health index that was used throughout this research was developed specifically for damage caused by the EAB. Some damage may be similar between EAB and ice storms, such as the appearance of epicormic branching [60]. On the other hand, disturbances such as ice storms can cause entire limbs of a tree to break off, whereas in an EAB infestation this may not occur until later stages of infestation when the tree is dead [5].

Although there was a two-year gap between image acquisition and field data collection, we are confident that the variation of infestation over space should remain similar, as the infestation of ash trees by the EAB is a slow process. This speculation is also confirmed by a comparison between the tree health data collected in the summers of 2014 and 2015. No significant differences are observed in the variables (*i.e.*, twig dieback, crown condition, and general tree health) between the two years ($p > 0.40$), although the ash health conditions observed in 2015 are slightly worse than those observed in 2014.

4. Conclusions and Future Work

Using two different types of segmentation methods, a multi-band watershed segmentation and a multiresolution segmentation, as well as the random forest classifier for classification, ash trees were successfully delineated and classified in EAB-infested natural forests. Although the results show that the watershed algorithm outperformed the multiresolution method greatly, the difference in the final classification maps produced from the two segmentation maps are not as obvious. Using an ash prediction model that was developed based on an ash health index and NDVI, an ash health map was successfully produced for the study area. The overall ash health map accuracy of 70% suggests that high spatial resolution multispectral images are capable of monitoring early ash decline as a result of EAB infestation.

Multispectral data with red-edge band and hyperspectral data have proven useful for monitoring and tracking infestations within conservation and urban areas [25,26]. Further work will employ these data to improve the prediction model, with the ultimate goal of accurately predicting ash health across space and time. Although the cost of the hyperspectral data from commercial suppliers may be prohibitive for some, the continuing advancement of Unmanned Aerial Vehicle (UAV) technology may provide a cheaper alternative. Future work will consider expanding the study area across Ontario to better capture the variation in EAB infestation. This may allow for the development of a general model that could be applied to a wide variety of forests.

Acknowledgments: This project is supported by an Early Researcher Award (ERA) from the provincial Ministry of Research and Innovation in Ontario, a Research and Scholarly Activity Fund from the University of Toronto Mississauga to Yuhong He, and the Department of Geography Undergraduate Research Assistantship and Undergraduate Research Grant Award at UTM to Justin Murfitt. The authors would also like to acknowledge Credit Valley Conservation for logistic support and undergraduate student Joel Jeyarajah for field data collection.

Author Contributions: Yuhong He formed the general idea of the paper, and conceived and designed the experiments. Justin Murfitt performed the field experiments, analyzed the field data, and wrote the draft under the direct supervision of Yuhong He. Jian Yang performed image segmentation and classification. Yuhong He, Amy Mui and Jian Yang helped edit the draft and provided critical comments to improve the paper. Kevin De Mille provided expertise in ash tree identification and assisted with field site selection.

Conflicts of Interest: The authors declare no conflict of interest.

Abbreviations

The following abbreviations are used in this manuscript:

UA	User's Accuracy
PA	Producer's Accuracy
EAB	Emerald Ash Borer
SEI	Segmentation Evaluation Index
WV2	WorldView-2
MA	Map Accuracy
NDVI	Normalized Difference Vegetation Index
GNDVI	Green Normalized Difference Vegetation Index
EVI	Enhanced Vegetation Index
IPVI	Infrared Percentage Vegetation Index
DVI	Difference Vegetation Index
RVI	Ratio Vegetation Index
RDVI	Renormalized Difference Vegetation Index
UAV	Unmanned Aerial Vehicle
RMSE	Root Mean Square Error
SVM	Support Vector Machine
GEOBIA	Geographic Object-Based Image Analysis
SAGA	System for Automated Geoscientific Analyses
ATCOR	Atmospheric and Topographic Correction

References

1. Agnecy, C.F.I. *RMD-13-01: Regulated Areas for Emerald Ash Borer (EAB) (Agrilus planipennis Fairmaire)*; Canadian Food Inspection Agency: Ottawa, ON, Canada, 2014.
2. Herms, D.A.; Gandhi, K.J.; Smith, A.; Cardina, J.; Knight, K.S.; Herms, C.P.; Long, R.P.; McCullough, D.G. Ecological impacts of emerald ash borer in forests of southeast Michigan. In Proceedings of the 20th U.S. Department of Agriculture Interagency Research Forum on Invasive Species, Annapolis, MD, USA, 13–16 January 2009; McManus, K.A., Gottschalk, K.W., Eds.; U.S. Department of Agriculture, Forest Service, Northern Research Station: Newtown, PA, USA, 2009; pp. 36–37.

3. Cipollini, D.; Wang, Q.; Whitehill, J.G.A.; Powell, J.R.; Bonello, P.; Herms, D.A. Distinguishing defensive characteristics in the phloem of ash species resistant and susceptible to emerald ash borer. *J. Chem. Ecol.* **2011**, *37*, 450–459. [CrossRef] [PubMed]
4. Colautti, R.I.; Bailey, S.A.; Van Overdijk, C.D.A.; Amundsen, K.; MacIsaac, H.J. Characterised and projected costs of nonindigenous species in Canada. *Biol. Invasions* **2006**, *8*, 45–59. [CrossRef]
5. Poland, T.M.; McCullough, D.G. Emerald ash borer: Invasion of the urban forest and the threat to North America's ash resource. *J. For.* **2006**, *104*, 118–124.
6. Smitley, D.; Davis, T.; Rebek, E. Progression of ash canopy thinning and dieback outward from the initial infestation of emerald ash borer (Coleoptera: Buprestidae) in southeastern Michigan. *J. Econ. Entomol.* **2008**, *101*, 1643–1650. [CrossRef] [PubMed]
7. Herms, D.A.; McCullough, D.G. Emerald ash borer invasion of North America: History, biology, ecology, impacts, and management. *Annu. Rev. Entomol.* **2014**, *59*, 13–30. [CrossRef] [PubMed]
8. Siegert, N.W.; McCullough, D.G.; Liebhold, A.M.; Telewski, F.W. Spread and dispersal of emerald ash borer: A dendrochronological approach. In Proceedings of the Emerald Ash Borer Research and Technology Development Meeting, Pittsburgh, PA, USA, 26–27 September 2010; p. 10.
9. McKenzie, N.; Helson, B.; Thompson, D.; Otis, G.; McFarlane, J.; Buscarini, T.; Meating, J. Azadirachtin: An effective systemic insecticide for control of *Agrilus planipennis* (Coleoptera: Buprestidae). *J. Econ. Entomol.* **2010**, *103*, 708–717. [CrossRef] [PubMed]
10. Hay, G.J.; Castilla, G. Geographic Object-Based Image Analysis (GEOBIA): A new name for a new discipline. In *Object-Based Image Analysis*; Springer: Berlin, Germany; Heidelberg, Germany, 2008; pp. 75–89.
11. Yang, J.; He, Y.; Weng, Q. An automated method to parameterize segmentation scale by enhancing intrasegment homogeneity and intersegment heterogeneity. *IEEE Geosci. Remote Sens. Lett.* **2015**, *12*, 1282–1286. [CrossRef]
12. Yang, J.; He, Y.; Caspersen, J. A multi-band watershed segmentation method for individual tree crown delineation from high resolution multispectral aerial image. In Proceedings of the IEEE International Geoscience and Remote Sensing System, Quebec City, QC, Canada, 13–18 July 2014; pp. 1588–1591.
13. Benz, U.C.; Hofmann, P.; Willhauck, G.; Lingenfelder, I.; Heynen, M. Multi-resolution, object-oriented fuzzy analysis of remote sensing data for GIS-ready information. *ISPRS J. Photogramm. Remote Sens.* **2004**, *58*, 239–258. [CrossRef]
14. Zhang, H.; Fritts, J.E.; Goldman, S.A. Image segmentation evaluation: A survey of unsupervised methods. *Comput. Vis. Image Underst.* **2008**, *110*, 260–280. [CrossRef]
15. Yang, J.; Li, P.; He, Y. A multi-band approach to unsupervised scale parameter selection for multi-scale image segmentation. *ISPRS J. Photogramm. Remote Sens.* **2014**, *94*, 13–24. [CrossRef]
16. Yang, J.; He, Y.; Caspersen, J.; Jones, T. A discrepancy measure for segmentation evaluation from the perspective of object recognition. *ISPRS J. Photogramm. Remote Sens.* **2015**, *101*, 186–192. [CrossRef]
17. Myint, S.W.; Gober, P.; Brazel, A.; Grossman-Clarke, S.; Weng, Q. Per-pixel *vs.* object-based classification of urban land cover extraction using high spatial resolution imagery. *Remote Sens. Environ.* **2011**, *115*, 1145–1161. [CrossRef]
18. Huang, C.; Davis, L.S.; Townshend, J.R.G. An assessment of support vector machines for land cover classification. *Int. J. Remote Sens.* **2002**, *23*, 725–749. [CrossRef]
19. Mountrakis, G.; Im, J.; Ogole, C. Support vector machines in remote sensing: A review. *ISPRS J. Photogramm. Remote Sens.* **2011**, *66*, 247–259. [CrossRef]
20. Roli, F.; Fumera, G. Support vector machines for remote sensing image classification. *Proc. SPIE* **2001**, *4170*, 160–166.
21. Duda, R.O.; Hart, P.E.; Stork, D.G. *Pattern Classification*, 2nd ed.; John Wiley & Sons, Inc.: New York, NY, USA, 2001.
22. Carter, G.A. Responses of leaf spectral reflectance to plant stress. *Am. J. Bot.* **1993**, *80*, 239–243. [CrossRef]
23. Carter, G.A. Ratios of leaf reflectances in narrow wavebands as indicators of plant stress. *Int. J. Remote Sens.* **1994**, *15*, 697–703. [CrossRef]
24. Bourque, D.P.; Naylor, A.W. Large effects of small water deficits on chlorophyll accumulation and ribonucleic acid synthesis in etiolated leaves of jack bean (*Canavalia ensiformis* [L.] DC.). *Plant Physiol.* **1971**, *47*, 591–594. [CrossRef] [PubMed]

25. Pontius, J.; Martin, M.; Plourde, L.; Hallett, R. Ash decline assessment in emerald ash borer-infested regions: A test of tree-level, hyperspectral technologies. *Remote Sens. Environ.* **2008**, *112*, 2665–2676. [CrossRef]
26. Zhang, K.; Hu, B.; Hanou, I.; Jin, L. Early detecting ash Emerald Ash Borer (EAB) infestation using Hyperspectral imagery. In Proceedings of the IEEE International Geoscience and Remote Sensing Symposium, Munich, Germany, 22–27 July 2012; pp. 6360–6363.
27. Waser, L.T.; Küchler, M.; Jütte, K.; Stampfer, T. Evaluating the potential of worldview-2 data to classify tree species and different levels of ash mortality. *Remote Sens.* **2014**, *6*, 4515–4545. [CrossRef]
28. Schomaker, M.E.; Zarnoch, S.J.; Bechtold, W.A.; Latelle, D.J.; Burkman, W.G.; Cox, S.M. *Crown-Condition Classification: A Guide to Data Collection and Analysis*; General Technical Report SRS-102. U.S. Department of Agriculture, Forest Service, Southern Research Station: Asheville, NC, USA, 2007.
29. Bendor, T.K.; Metcalf, S.S.; Fontenot, L.E.; Sangunett, B.; Hannon, B. Modeling the spread of the Emerald Ash Borer. *Ecol. Model.* **2006**, *7*, 221–236. [CrossRef]
30. Jennings, S.B.; Brown, N.D.; Sheil, D. Assessing forest canopies and understorey illumination: Canopy closure, canopy cover and other measures. *Forestry* **1999**, *72*, 59–73. [CrossRef]
31. Demarez, V.; Duthoit, S.; Baret, F.; Weiss, M.; Dedieu, G. Estimation of leaf area and clumping indexes of crops with hemispherical photographs. *Agric. For. Meteorol.* **2008**, *148*, 644–655. [CrossRef]
32. Rossini, M.; Panigada, C.; Meroni, M.; Colombo, R. Assessment of oak forest condition based on leaf biochemical variables and chlorophyll fluorescence. *Tree Physiol.* **2006**, *26*, 1487–1496. [CrossRef] [PubMed]
33. Laben, C.A.; Brower, B.V. Process for Enhancing the Spatial Resolution of Multispectral Imagery Using Pansharpening. U.S. Patent 611875, 4 January 2000.
34. Li, C.; Liu, L.; Wang, J.; Zhao, C.; Wang, R. Comparison of two methods of the fusion of remote sensing images with fidelity of spectral information. In Proceedings of the IEEE International Geoscience and Remote Sensing Symposium, Anchorage, AK, USA, 20–24 September 2004; pp. 2561–2564.
35. Blaschke, T.; Geoffrey, J. Obect-oriented image analysis and scale-space: Theory and methods and evaluating multiscale lanscape structure. *Int. Arch. Photogramm. Remote Sens.* **2001**, *34*, 22–29.
36. Conrad, O.; Bechtel, B.; Bock, M.; Dietrich, H.; Fischer, E.; Gerlitz, L.; Wehberg, J.; Wichmann, V.; Böhner, J. System for Automated Geoscientific Analyses (SAGA) v. 2.1.4. *Geosci. Model Dev. Discuss.* **2015**, *8*, 2271–2312. [CrossRef]
37. Definiens AG. *Definiens Developer 7 User Guide*; Definiens AG: Munchen, Germany, 2009.
38. Jackson, R.D.; Huete, A.R. Interpreting vegetation indices. *Prev. Vet. Med.* **1991**, *11*, 185–200. [CrossRef]
39. Ahamed, T.; Tian, L.; Zhang, Y.; Ting, K.C. A review of remote sensing methods for biomass feedstock production. *Biomass Bioenergy* **2011**, *35*, 2455–2469. [CrossRef]
40. Huete, A.; Didan, K.; Miura, T.; Rodriguez, E.P.; Gao, X.; Ferreira, L.G. Overview of the radiometric and biophysical performance of the MODIS vegetation indices. *Remote Sens. Environ.* **2002**, *83*, 195–213. [CrossRef]
41. Crippen, R.E. Calculating the vegetation index faster. *Remote Sens. Environ.* **1990**, *73*, 71–73. [CrossRef]
42. Tucker, C.J. Red and photographic infrared linear combinations for monitoring vegetation. *Remote Sens. Environ.* **1979**, *150*, 127–150. [CrossRef]
43. Jordan, C.F. Derivation of leaf-area index from quality of light on the forest floor. *Ecology* **1969**, *50*, 663–666. [CrossRef]
44. Roujean, J.L.; Breon, F.M. Estimating PAR absorbed by vegetation from bidirectional reflectance measurements. *Remote Sens. Environ.* **1995**, *51*, 375–384. [CrossRef]
45. Baugh, W.M.; Groeneveld, D.P. Broadband vegetation index performance evaluated for a low-cover environment. *Int. J. Remote Sens.* **2006**, *27*, 4715–4730. [CrossRef]
46. Team, R.C. *R: A Language and Environmnet for Statistical Computing*; R Foundation for Statistical Computing: Vienna, Austria, 2013.
47. Pu, R.; Gong, P. Wavelet transform applied to EO-1 hyperspectral data for forest LAI and crown closure mapping. *Remote Sens. Environ.* **2004**, *91*, 212–224. [CrossRef]
48. Latif, Z.A.; Zamri, I.; Omar, H. Determination of tree species using Worldview-2 data. In Proceedings of the IEEE 8th International Colloquium on Signal Processing and its Applications, Malacca, Malaysia, 23–25 March 2012; pp. 383–387.
49. Katoh, M. Classifying tree species in a northern mixed forest using high-resolution IKONOS data. *J. For. Res.* **2004**, *9*, 7–14. [CrossRef]

50. Immitzer, M.; Atzberger, C.; Koukal, T. Tree species classification with random forest using very high spatial resolution 8-band WorldView-2 satellite data. *Remote Sens.* **2012**, *4*, 2661–2693. [CrossRef]
51. Doody, T.M.; Lewis, M.; Benyon, R.G.; Byrne, G. A method to map riparian exotic vegetation (*Salix* spp.) area to inform water resource management. *Hydrol. Process.* **2014**, *28*, 3809–3823. [CrossRef]
52. Omer, G.; Mutanga, O.; Abdel-Rahman, E.M.; Adam, E. Performance of support vector machines and artifical neural network for mapping endangered tree species using WorldView-2 data in Dukuduku Forest, South Africa. *IEEE J. Sel. Top. Appl. Earth Obs. Remote Sens.* **2015**, *8*, 4825–4840. [CrossRef]
53. Dalponte, M.; Ørka, H.O.; Gobakken, T.; Gianelle, D.; Næsset, E. Tree species classification in boreal forests with hyperspectral data. *IEEE Trans. Geosci. Remote Sens.* **2013**, *51*, 2632–2645. [CrossRef]
54. Pu, R.; Landry, S. A comparative analysis of high spatial resolution IKONOS and WorldView-2 imagery for mapping urban tree species. *Remote Sens. Environ.* **2012**, *124*, 516–533. [CrossRef]
55. Oumar, Z.; Mutanga, O. Integrating environmental variables and WorldView-2 image data to improve the prediction and mapping of Thaumastocoris peregrinus (bronze bug) damage in plantation forests. *ISPRS J. Photogramm. Remote Sens.* **2014**, *87*, 39–46. [CrossRef]
56. Immitzer, M.; Atzberger, C. Early detection of bark beetle infestation in Norway spruce (*Picea abies*, L.) using WorldView-2 data. *Photogramm. Fernerkundung Geoinform.* **2014**, *2014*, 351–367. [CrossRef]
57. Chávez, R.O.; Clevers, J.G.P.W. *Object-Based Analysis of 8-Bands Worldview2 Imagery for Assessing Health Condition of Desert Trees*; Wageningen University: Wageningen, The Netherlands, 2012.
58. Filchev, L. An assessment of european spruce bark beetle infestation using WorldView-2 Satellite data. In Proceedings of the 1st European SCGIS Conference with International Participation "Best Practices: Application of GIS Technologies for Conservation of Natural and Cultural Heritage Sites", Sofia, Bulgaria, 21–23 May 2012; pp. 21–23.
59. Chapin, F.S. Integrated responses of plants to stress. *Bioscience* **1991**, *41*, 29–36. [CrossRef]
60. Turcotte, R.M.; Elliott, T.R.; Fajvan, M.A.; Park, Y.; Snider, D.A.; Tobin, P.C. Effects of ice storm damage on hardwood survival and growth in Ohio. *North. J. Appl. For.* **2012**, *29*, 53–59. [CrossRef]